https://doi.org/10.5194/egusphere-2026-5344
Preprint. Discussion started: 18 November 2026
© Author(s) 2026. CC BY 4.0 License.

ASIS : the Auroral Spectrograph In Skibotn

Hervé Lamy[1], Gaël Cessateur[1], David Bolsée[1], Mathieu Barthelemy[2], and Magnar Gullikstad Johnsen[3]

[1]Royal Belgian Institute for Space Aeronomy, Avenue Circulaire 3, 1180 Uccle, Belgium
[2]Univ. Grenoble Alpes, CNRS, IPAG, 38000 Grenoble, France
[3]Tromsø Geophysical Observatory, Faculty of Science and Technology, UiT the Arctic University of Norway, N-9037 Tromsø, Norway

Correspondence: Hervé Lamy (herve.lamy@aeronomie.be)

Abstract. ASIS (Auroral Spectrograph In Skibotn) is a ground-based spectrograph designed for continuous monitoring and quantitative characterization of visible auroral emissions. Installed at Skibotn Observatory in northern Norway, the instrument uses a commercial Czerny–Turner spectrograph with interchangeable gratings, providing either broad spectral coverage or higher spectral dispersion for dedicated observations of selected auroral features. In its standard configuration, ASIS covers approximately 405-687 nm with a spectral resolution of about 1.2 nm and a temporal resolution of 30 s. We describe the instrument architecture, including the collecting optics, spectrograph–detector assembly, field-of-view characterization, and automated control and data acquisition, together with its wavelength and radiometric calibration. Absolute radiometric response curves were derived from calibrated FEL lamps using grating-specific calibration configurations, allowing measured spectra to be converted into absolute spectral brightness in Rayleigh units. Wavelength calibration was performed using Hg–Ar and Ne emission lamps and second-order polynomial fits. Calibrated observations demonstrate the capability of ASIS to resolve the main atomic and molecular auroral emissions, including the N_2^+ first negative bands, the O(^{1}S) and O(^{1}D) lines, and Balmer emissions associated with proton precipitation. The calibrated intensities and line ratios can be used to constrain the characteristic energy of precipitating particles and to support coordinated multi-instrument studies of auroral dynamics and energy deposition.

1 Introduction

Ground-based auroral spectroscopy remains one of the most powerful tools for diagnosing magnetosphere–ionosphere coupling and upper atmospheric response to particle precipitation. By resolving discrete atomic and molecular emissions—most prominently the atomic oxygen lines at 557.7 nm and 630.0 nm and the N_2 and N_2^+ band systems—spectroscopic measurements provide quantitative constraints on excitation altitude, characteristic energy of precipitating particles, thermospheric temperature, and neutral winds (Chamberlain, 1961; Vallance Jones, 1974; Rees, 1989).

Over the past decades, major instrumental developments have transformed auroral spectroscopy from single-channel scanning photometers to multi-line imaging spectrographs and high-resolution Doppler instruments. In Canada, the Transition Region Explorer (TREx) network has deployed advanced narrowband imagers and spectrographic systems designed to resolve fine-scale auroral dynamics and transition-region physics. Beyond instrumental innovation, TREx has enabled major scientific

https://doi.org/10.5194/egusphere-2026-5344
Preprint. Discussion started: 18 November 2026
© Author(s) 2026. CC BY 4.0 License.

advances, notably the first detailed spectroscopic characterization of the optical emissions associated with the phenomenon known as STEVE (Strong Thermal Emission Velocity Enhancement). Observations reported by Gillies et al. (2019) demonstrated that STEVE is dominated by a broadband continuum emission distinct from classical auroral precipitation, with weak or absent signatures of typical auroral lines such as 557.7 nm. These results provided compelling evidence that STEVE arises from subauroral ion drifts and extreme ionospheric heating rather than conventional particle precipitation.

At high latitudes, the Svalbard region hosts several long-running optical facilities colocated with radar infrastructure such as EISCAT, allowing coordinated optical–radar studies. Spectrographic and Fabry–Pérot interferometer measurements at Kjell Henriksen Observatory (KHO) and related sites have provided high-resolution observations of thermospheric temperatures and winds derived from auroral and airglow emissions (Conde and Smith, 1995, 1997). The synergy between optical spectroscopy and incoherent scatter radar measurements has been particularly important for validating energy deposition estimates and ionospheric heating models. More recently, Tsuda et al. (2020) deployed a temporary spectrographic system near EISCAT and reported detailed spectral observations of unusual auroral structures, highlighting strong subauroral ion drift signatures and atypical emission characteristics. Their results further emphasized the importance of coordinated optical and radar diagnostics for disentangling particle-driven aurora from electrodynamic heating processes.

High-dispersion spectroscopic systems such as the High Throughput Imaging Echelle Spectrograph (HiTIES) have further advanced the field by enabling simultaneous high spectral resolution and spatial coverage (Chakrabarti et al., 2001; Partamies et al., 2025). These instruments are capable of resolving fine Doppler structure in auroral emission lines, allowing precise retrieval of neutral temperatures, wind velocities, and, in some cases, non-thermal line broadening associated with dynamic auroral processes.

Collectively, these instrumental efforts demonstrate that modern auroral spectroscopy not only refines quantitative diagnostics of classical auroral precipitation but also enables the identification of fundamentally different energy deposition mechanisms, such as subauroral ion drift heating. They highlight the importance of rigorous calibration, accurate instrumental line shape characterization, and coordinated multi-instrument campaigns. Contemporary studies increasingly rely on cross-validation with all-sky imaging, incoherent scatter radar (e.g., EISCAT), and satellite-based particle measurements (e.g., THEMIS, DMSP), reinforcing the central role of optical spectroscopy as the quantitative bridge between observed emissions and modeled particle precipitation spectra.

In this study, we present ASIS (Auroral Spectrograph In Skibotn), a grating spectrograph optimized for observations in the 400–$700\,\mathrm{nm}$ spectral range, with a spectral resolution of $\Delta\lambda \sim 1.2\,\mathrm{nm}$ and a temporal resolution of $\Delta t = 30\,\mathrm{s}$. Although based on commercially available optical and spectroscopic components, ASIS has been specifically configured and integrated for long-term autonomous auroral observations at Skibotn Observatory. Its combination of automated operation, broad spectral coverage, and absolute radiometric calibration provides a reliable framework for quantitative auroral spectroscopy and coordinated multi-instrument studies. Section 2 presents the ASIS instrument architecture, including the collecting optics and field-of-view characterization, the spectrograph–detector assembly, the observing modes and automated acquisition procedures, and the main technical characteristics of the system. Section 3 presents the radiometric calibration, including the instrumental response and the conversion to absolute spectral brightness in Rayleighs. Section 4 describes the wavelength cal-

https://doi.org/10.5194/egusphere-2026-5344
Preprint. Discussion started: 18 November 2026
© Author(s) 2026. CC BY 4.0 License.

ibration. In Section 5, we present a series of calibrated auroral spectra and discuss key scientific applications, demonstrating the instrument's capability to provide improved quantitative constraints on auroral energy deposition.

2 Description of the instrument

2.1 General overview

ASIS is a ground-based optical instrument designed for routine visible spectroscopy of auroral emissions. The system is installed at Skibotn Observatory, northern Norway (lat. $\sim 69.3^\circ$ N, long. $\sim 20.2^\circ$ E), and has been operating since October 2023. ASIS is not a custom-built monolithic spectrograph, but an integrated observing system assembled from commercial optical and spectroscopic subsystems dedicated to continuous auroral monitoring.

The instrument consists of two main parts: (1) a light-collecting assembly that views the sky through an acrylic dome and injects the collected light into an optical fiber, and (2) a spectrograph–detector unit based on an Andor SR-303i Czerny–Turner spectrograph coupled to an Andor iDus CCD detector. The optical configuration of ASIS is illustrated in Fig. 1.

2.2 Light-collecting assembly and fiber coupling

The sky signal is collected by an astronomical lens with a clear aperture of 60 mm and a focal length of 248 mm. In the standard observing configuration, this optical system provides a circular field of view of approximately 4°. The angular response of the collecting optics was characterized in the laboratory using a 4 mm diameter pinhole illuminated by a FEL lamp. The collected light was transmitted through a 600 μm core optical fiber and measured using a silicon photodiode. A spare telescope with identical optical configuration was rotated over an angular range of $\pm 6^\circ$ in steps of 10 arcmin. The pinhole was located approximately 101.2 cm from the effective rotation centre, corresponding to an angular source diameter of 13.6 arcmin. The measured response exhibits a nearly flat plateau with sharp edges, yielding a full width at half maximum of approximately 4°.

The line of sight is fixed and oriented approximately along the local magnetic field line, at an elevation of about 78° and an azimuth of about 183° (southward direction). Figure 2 illustrates the pointing direction and field of view of ASIS on an all-sky image recorded at Skibotn Observatory during auroral activity.

The light collected by the lens is transferred to the spectrograph through a 600 μm core optical fiber connected via an SMA interface. A reflective coupling optic with a diameter of 22 mm is mounted behind the lens to focus the collected light into the fiber. This arrangement allows the collecting optics and the spectrograph to be mechanically separated, while preserving stable optical coupling and operational flexibility.

The observing head is located under an acrylic dome that protects the instrument from the Arctic environment. The dome was not included in the direct on-site calibration measurements; its transmission was therefore accounted for separately. Based on manufacturer specifications, the dome transmittance is approximately constant at 92% between 400 and 1000 nm.

https://doi.org/10.5194/egusphere-2026-5344
Preprint. Discussion started: 18 November 2026
© Author(s) 2026. CC BY 4.0 License.

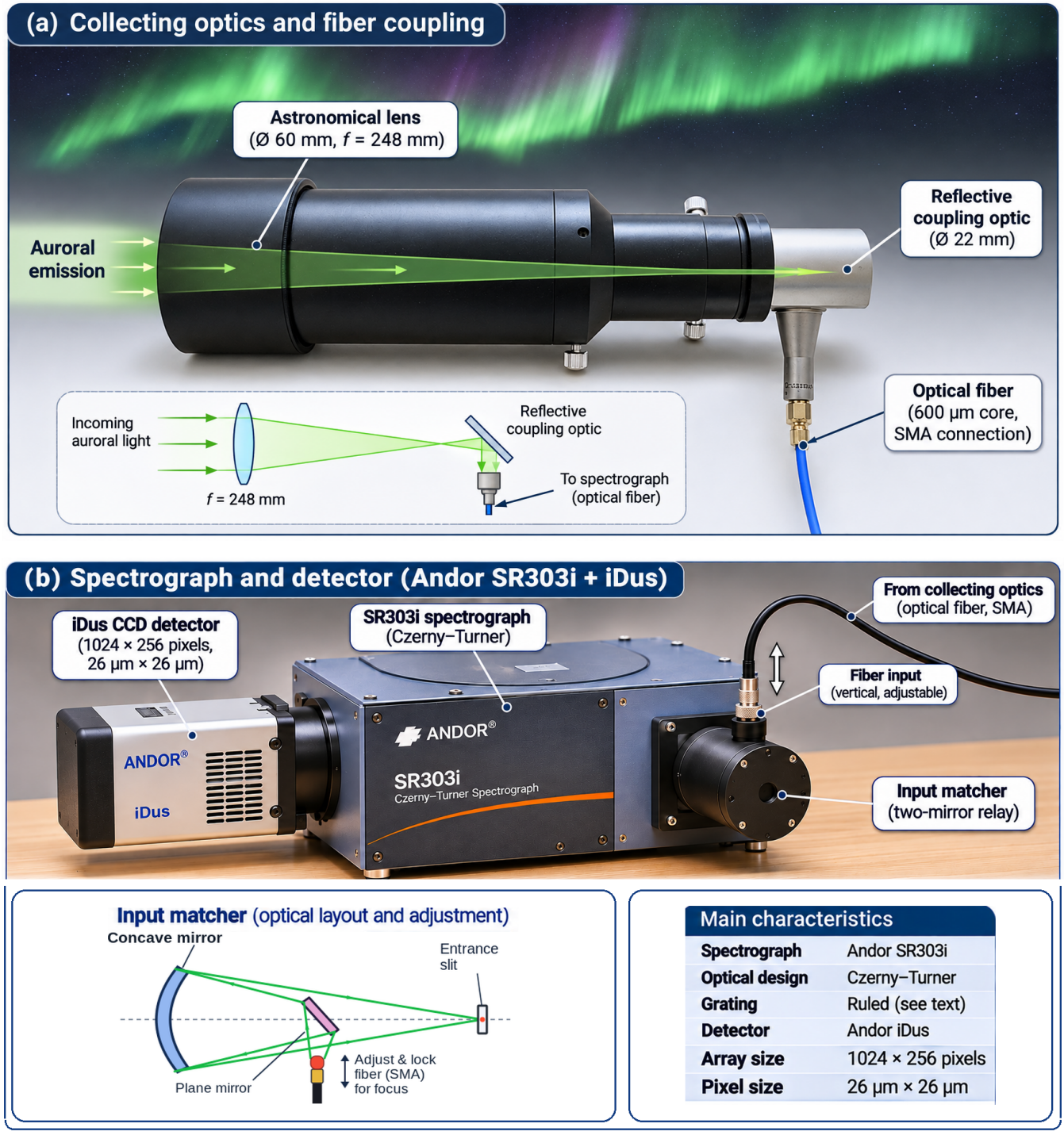


Figure 1. Optical configuration of the ASIS instrument. (a) Collecting optics and fiber coupling. (b) Andor SR303i spectrograph, input matcher, and iDus CCD detector.

https://doi.org/10.5194/egusphere-2026-5344
Preprint. Discussion started: 18 November 2026
© Author(s) 2026. CC BY 4.0 License.

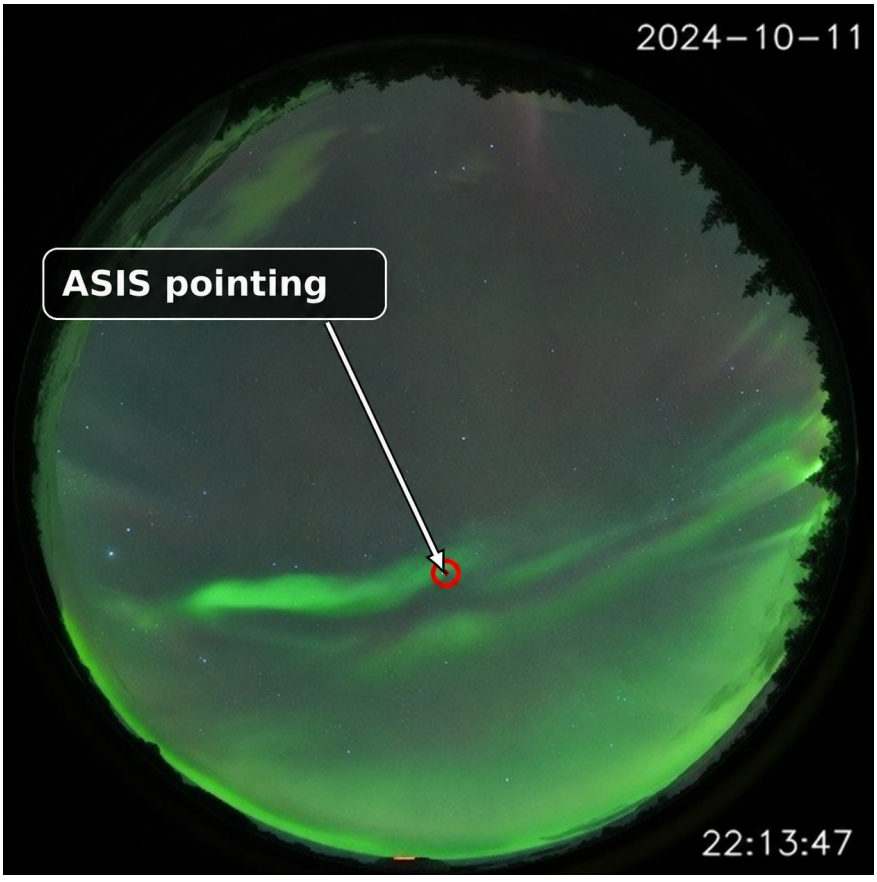


Figure 2. All-sky image recorded at Skibotn Observatory on 11 October 2024 at 22:13:47, showing auroral emissions and the ASIS pointing direction (red circle). The instrument has a circular field of view of approximately 4°, centred at an elevation of 78° and an azimuth of 183°. The all-sky image was provided by Dr. Sota Nanjo. The Skibotn all-sky camera is described in Nanjo et al. (2026).

2.3 Spectrograph and detector

The spectrograph used in ASIS is a commercial Andor SR-303i imaging spectrograph based on a Czerny–Turner optical design. It has a focal length of 303 mm, an f/4 aperture, and a motorized entrance slit adjustable from 10 μm to 2.5 mm. The grating turret can accommodate three interchangeable gratings with groove densities of 300, 600, and 1800 lines mm^{-1}, enabling operation at different spectral dispersions according to the scientific objective.

In practice, the ASIS observations presented here rely mainly on two observing configurations. Grating 1 (300 lines mm^{-1}) is used as the standard monitoring mode because it provides broad spectral coverage over approximately 405–687 nm with a dispersion of about 0.3 nm pixel^{-1}. Grating 3 (1800 lines mm^{-1}) is used for dedicated high-dispersion observations of selected auroral features, with a dispersion of about 0.05 nm pixel^{-1} over a narrower spectral interval.

https://doi.org/10.5194/egusphere-2026-5344
Preprint. Discussion started: 18 November 2026
© Author(s) 2026. CC BY 4.0 License.

The optical fiber is connected to the spectrograph through an adjustable input matcher (Andor SR-ASM-0038) incorporating two mirrors. A plane mirror tilted at 45° redirects the light emerging from the fiber toward a concave mirror, which focuses the fiber output onto the spectrograph entrance slit. The fiber position can be adjusted vertically to optimize the focus, while the alignment of the concave mirror can be manually adjusted to maximize optical throughput. The input matcher has a nominal magnification of 1.8 and an f/4 optical configuration, matching the f-number of the SR303i spectrograph.

The detector is a 16-bit Andor iDus CCD camera with a 1024×256 pixel array. The detector is thermoelectrically cooled by a Peltier system, typically operated at $-70°$C, in order to reduce dark current and readout noise during long integrations.

2.4 Instrument operation and observing modes

Routine observations are automatically scheduled by a dedicated Python script that computes the daily solar ephemerides and determines the observing interval during which the solar elevation remains below $-15°$. The number of exposures is calculated from the duration of this interval and the selected exposure time. The script then launches Andor SOLIS, the manufacturer software interface which controls the SR-303i spectrograph and the iDus CCD, with the appropriate acquisition parameters, including grating selection, slit width, exposure time, readout mode, and number of exposures. The acquired data are stored locally at the observatory and automatically transferred once per day to the servers of the Royal Belgian Institute for Space Aeronomy (BIRA-IASB). The data acquisition architecture of ASIS is illustrated in Fig. 3.

Since its installation, ASIS has been operated primarily in a standard monitoring configuration using Grating 1, a slit width of 100 μm, an exposure time of 30 s, and full vertical binning (FVB) of the CCD. In this configuration, the instrument covers the approximate wavelength range 405–687 nm with a spectral resolution of about 1.2 nm, estimated from the full width at half maximum of emission lines. The FVB mode is used to integrate the total signal recorded along the slit and maximize sensitivity for auroral monitoring.

Dedicated campaigns may also use Grating 3 in order to focus on narrower spectral intervals around selected auroral emissions such as the N_2^+ 427.8 nm band, the OI 557.7 nm line, the OI 630.0/636.4 nm lines, Hα, or the OI 777.4 nm multiplet.

2.5 Installation, interfaces, and practical implementation

ASIS is assembled from commercial subsystems integrated at the Skibotn observatory for long-term autonomous operation. The system includes the external collecting optics, the fiber-fed spectrograph, the CCD detector, and the control computer. The modular architecture simplifies maintenance and reconfiguration, for example when changing the grating or switching between monitoring and dedicated high-dispersion observing modes.

The main optical, mechanical, and operational characteristics of ASIS are summarized in Table 1, including the specifications of its principal commercial subsystems.

Photographs of the collecting optics, spectrograph–detector assembly, and input matcher are shown in Fig. 4.

https://doi.org/10.5194/egusphere-2026-5344
Preprint. Discussion started: 18 November 2026
© Author(s) 2026. CC BY 4.0 License.

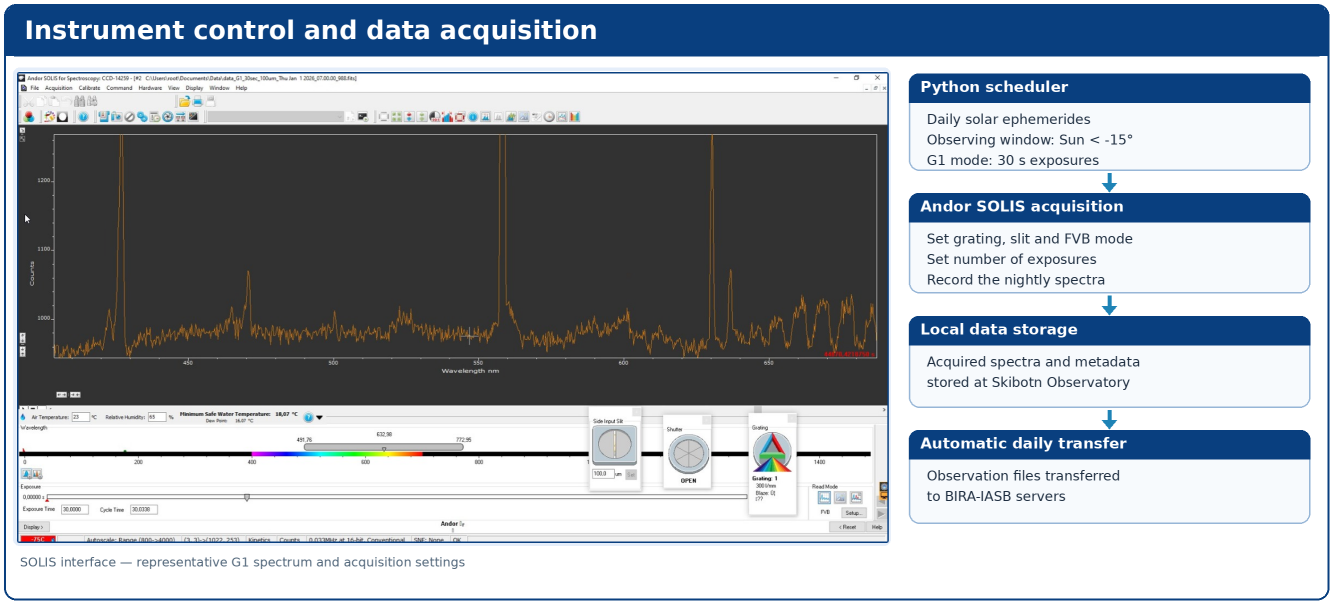


Figure 3. Instrument control and data acquisition architecture. The acquisition is automatically configured using a Python scheduler, and data are transferred daily to BIRA-IASB servers. The software screenshot was captured by the authors using Andor SOLIS spectroscopy software (Oxford Instruments Andor; https://andor.oxinst.com/products/solis-software/solis-s). The acquisition workflow diagram was prepared by the authors.

3 Radiometric calibration

3.1 General radiometric calibration procedure

Since the spectrograph and detector were already installed in Skibotn as part of a previous instrument configuration (Barthelemy et al., 2019), the radiometric calibration of ASIS was carried out on site in February 2024 and October 2024 using two FEL-type tertiary standards of spectral irradiance (1000 W quartz-halogen lamps). The transfer from secondary to tertiary standards was performed at the Belgian Radiometric Characterization Laboratory (B.RCLab[1]) at BIRA-IASB. The nominal operating current of the FEL lamps is 8 A, stabilized within 1 mA, using a Keysight N5770A power supply. Under these conditions, the lamp spectral irradiance is stable to within typically 0.2 %. An example of spectral irradiance (in mW m^{-2} nm^{-1}) provided by the FEL Lamp 1 powered at 8 A and located at 50 cm of the entrance optics / receiver is shown in Fig. 5.

The lamps were carefully aligned along the optical axis of the astronomical lens using a laser reference and a reticle to ensure precise positioning, with a lamp–astronomical lens distance of 99 cm. This setup allowed characterization of the spectral response of the entire instrument, excluding the acrylic dome. The dome transmittance, based on the manufacturer's specifications, was found to be approximately constant at 92% between 400 and 1000 nm.

[1]https://brclab.aeronomie.be/

https://doi.org/10.5194/egusphere-2026-5344
Preprint. Discussion started: 18 November 2026
© Author(s) 2026. CC BY 4.0 License.

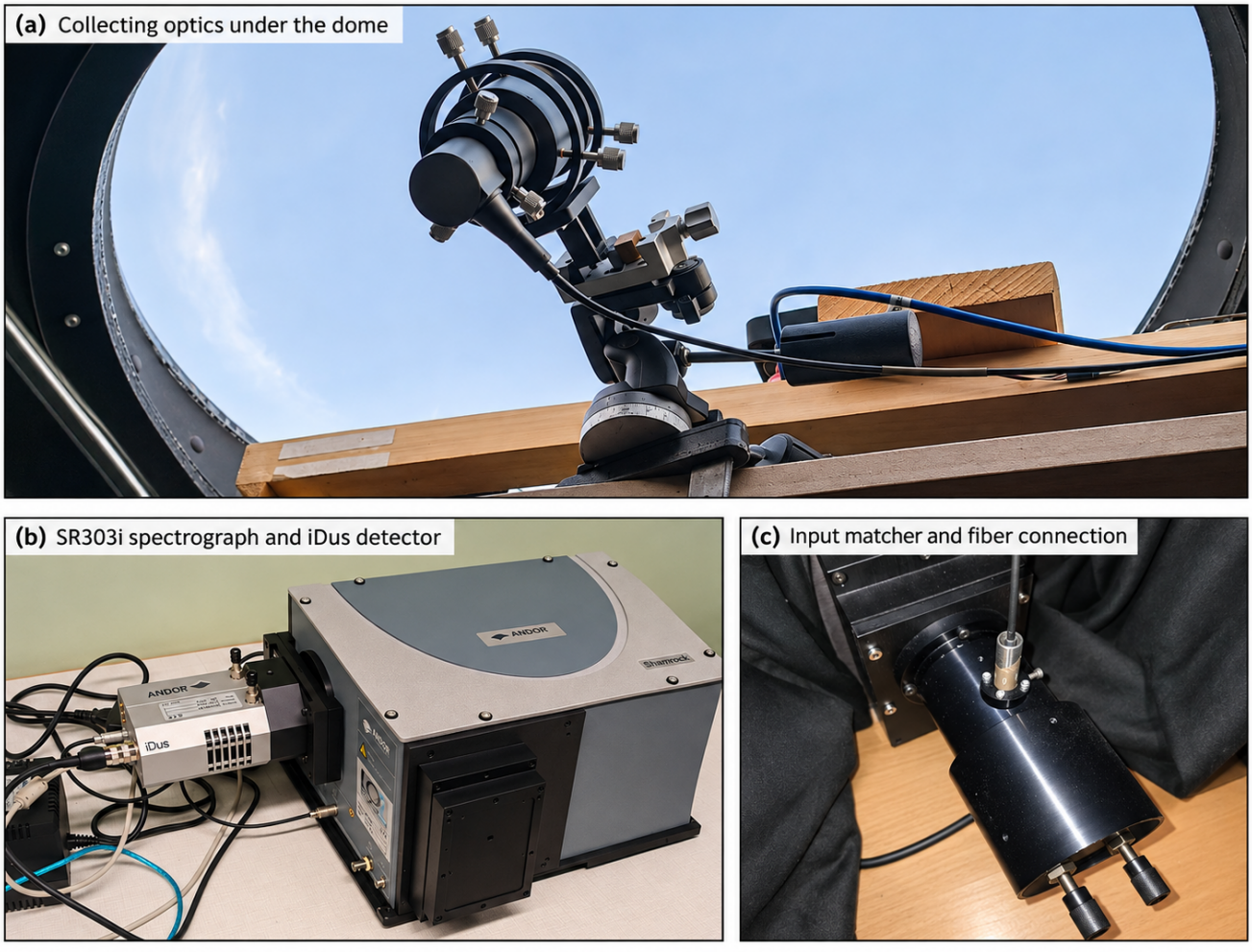


Figure 4. Photographs of the ASIS instrument. (a) Light-collecting telescope installed beneath the observatory dome at Skibotn, showing the optical fiber connection. (b) Andor SR303i spectrograph coupled to the iDus CCD detector, photographed at BIRA-IASB before installation in Skibotn and without the input matcher. (c) Input matcher installed at Skibotn Observatory, showing the optical fiber connection and mechanical adjustments.

https://doi.org/10.5194/egusphere-2026-5344
Preprint. Discussion started: 18 November 2026
© Author(s) 2026. CC BY 4.0 License.

Table 1. Main technical characteristics of the ASIS instrument.

Subsystem	Component	Main characteristics
Location	Skibotn Observatory	69.3° N, 20.2° E; installed in October 2023
Collecting optics	Astronomical lens	60 mm aperture; 248 mm focal length
Field of view	Fixed pointing	Circular FoV $\sim 4°$; elevation $\sim 78°$; azimuth $\sim 183°$
Coupling optics	Reflective optic	22 mm diameter; fiber injection
Optical fiber	SMA-coupled fiber	600 μm core diameter
Spectrograph	Andor SR-303i	Czerny–Turner design; 303 mm focal length; $f/4$
Entrance slit	Motorized	10 μm to 2.5 mm; nominal width 100 μm
Diffraction gratings	Motorized turret	300, 600 and 1800 lines mm^{-1}
Detector	Andor iDus CCD	1024 $\times$ 256 pixels; 16-bit digitization
Cooling	Thermoelectric (Peltier)	Operating temperature $-70\,°$C
Readout	Full Vertical Binning	Integration along the spatial dimension
Standard mode (G1)	300 lines mm^{-1}	405–687 nm; 0.3 nm pixel^{-1}; spectral resolution ~ 1.2 nm
High-dispersion mode (G3)	1800 lines mm^{-1}	Selected spectral windows (~ 40 nm); dispersion ~ 0.05 nm pixel^{-1}
Protective dome	Acrylic	Transmittance $\sim 92\,\%$ (400–1000 nm)
Instrument control	Software / Python	Automated acquisition; grating, slit, shutter and detector control
Input matcher	Andor SR-ASM-0038	$f/4$; NA = 0.125; acceptance angle $14.4°$; magnification 1.8; reference distance 66–68 mm
Spectrograph dimensions	Andor SR303i	394 $\times$ 283 $\times$ 208 mm
Spectrograph mass	Andor SR303i	Approximately 20 kg
Detector dimensions	Andor iDus	Approximately 156 mm length; 100 $\times$ 101 mm mounting face
Detector power supply	Andor PS-25	5 V DC (15 W); 7.5 V DC (30 W); $\pm$15 V DC (3 W)

All measurements were performed within the linear response regime of the system, both in terms of exposure time (typically ≥ 1 s) and recorded signal levels (maximum intensities $\leq 60{,}000$ ADU). Each measurement was repeated at least 20 consecutive times to assess the stability of the whole system, and the results were then averaged to increase signal-to-noise ratio (SNR). The room was darkened as much as possible to minimize stray light. Dark frames (with the camera's mechanical shutter closed) were obtained under the same conditions.

The calibration curve is derived using the following expression:

https://doi.org/10.5194/egusphere-2026-5344
Preprint. Discussion started: 18 November 2026
© Author(s) 2026. CC BY 4.0 License.

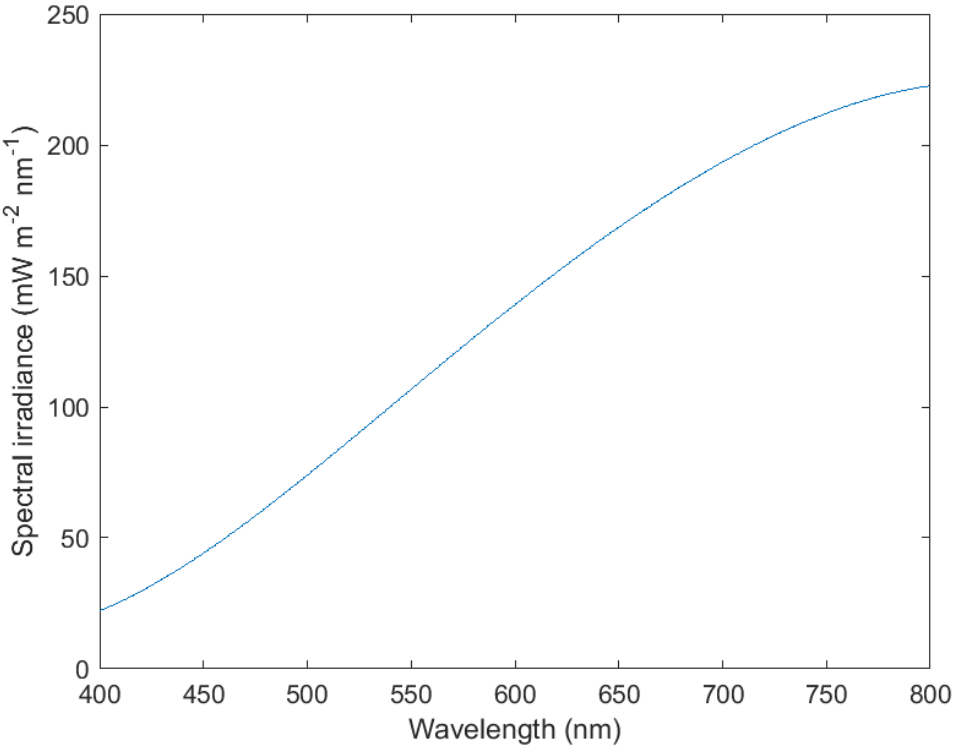


Figure 5. Reference spectral irradiance of FEL Lamp 1 operated at 8 A, measured at a distance of 50 cm from the lamp.

$$R(\lambda) = \frac{E(\lambda)}{T_d \frac{I_{\mathrm{ADU}}(\lambda)}{\Delta t}} \tag{1}$$

where $E(\lambda)$ denotes the spectral irradiance of the calibration lamp, T_d the dome transmittance, and $I_{\mathrm{ADU}}(\lambda)$ the measured signal (in ADU) obtained for an exposure time Δt, after correction for the dark current.

Neutral density (ND) filters were used to reduce the incoming flux and prevent detector saturation. The spectral irradiance of the calibration lamp, $E_{\mathrm{lamp}}(\lambda)$, corresponds to the value measured at the B.RCLab at 50 cm distance from the source, corrected for both the spectral attenuation of the neutral filters, $T_{\mathrm{ND}}(\lambda)$, and the geometrical dilution factor due to the lamp–instrument distance (inverse square law):

$$E(\lambda) = E_{\mathrm{lamp}}(\lambda) \times T_{\mathrm{ND}}(\lambda) \times \left(\frac{50}{99}\right)^2 \tag{2}$$

https://doi.org/10.5194/egusphere-2026-5344
Preprint. Discussion started: 18 November 2026
© Author(s) 2026. CC BY 4.0 License.

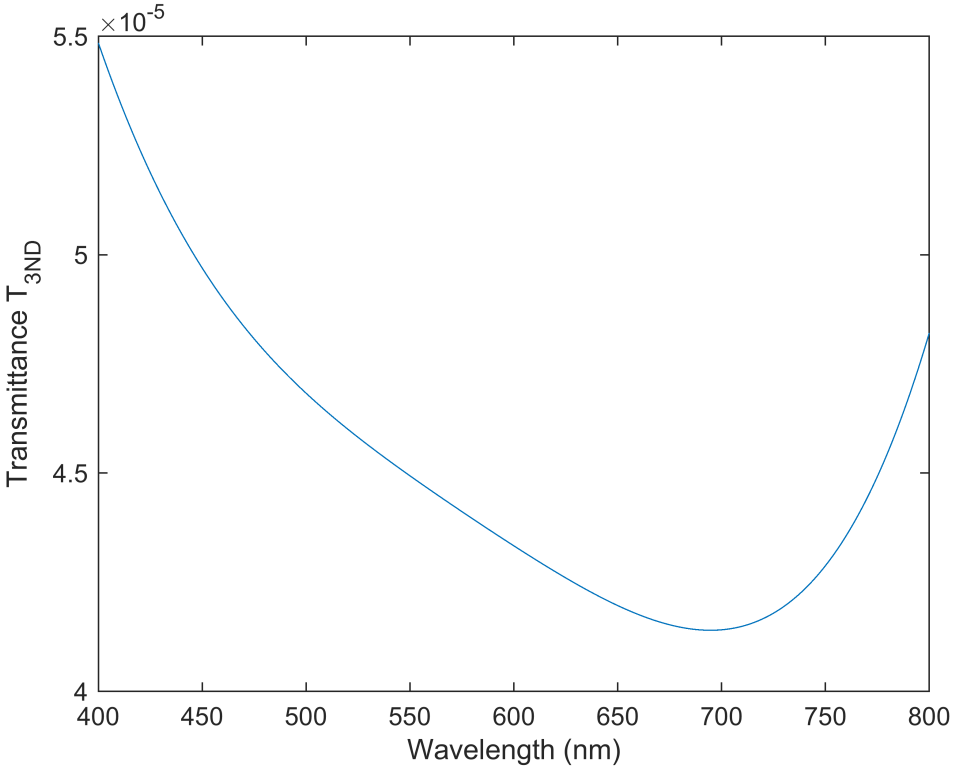


Figure 6. Transmittance of the combined ND filters as function of wavelength.

3.2 Grating 1

In February 2024, Grating 1 was calibrated. The camera and spectrograph parameters were identical to those described in Section 2. A range of exposure times was used during the calibration procedure. Three ND filters with attenuation factors of 8, 32 and 100 were stacked together in the optical path to reduce the incoming flux and prevent detector saturation. The ND32 filter was slightly tilted to avoid appearance of interference fringes in the observed spectra. The transmittance of the combined ND filter assembly, $T_{3\mathrm{ND}}$, was subsequently characterized in the B.RCLab and is shown in Fig. 6.

The spectral irradiance of the calibration lamp was obtained using equation 2 with $E_{\mathrm{lamp}}(\lambda) = E_{8\mathrm{A}}$ and $T_{\mathrm{ND}}(\lambda) = T_{3\mathrm{ND}}$. An example of the recorded signal obtained with FEL Lamp 1 operated at 8 A for various exposure times is shown inFig. 7.

Figure 8 shows an example of the calibration curves obtained for FEL Lamp 1 operated at 8 A, with exposure times ranging from 1 to 8 s. The resulting curves overlap closely, demonstrating the consistency of the measurements. Similar results were obtained with FEL Lamp 2, providing confidence in the robustness of the calibration procedure.

https://doi.org/10.5194/egusphere-2026-5344
Preprint. Discussion started: 18 November 2026
© Author(s) 2026. CC BY 4.0 License.

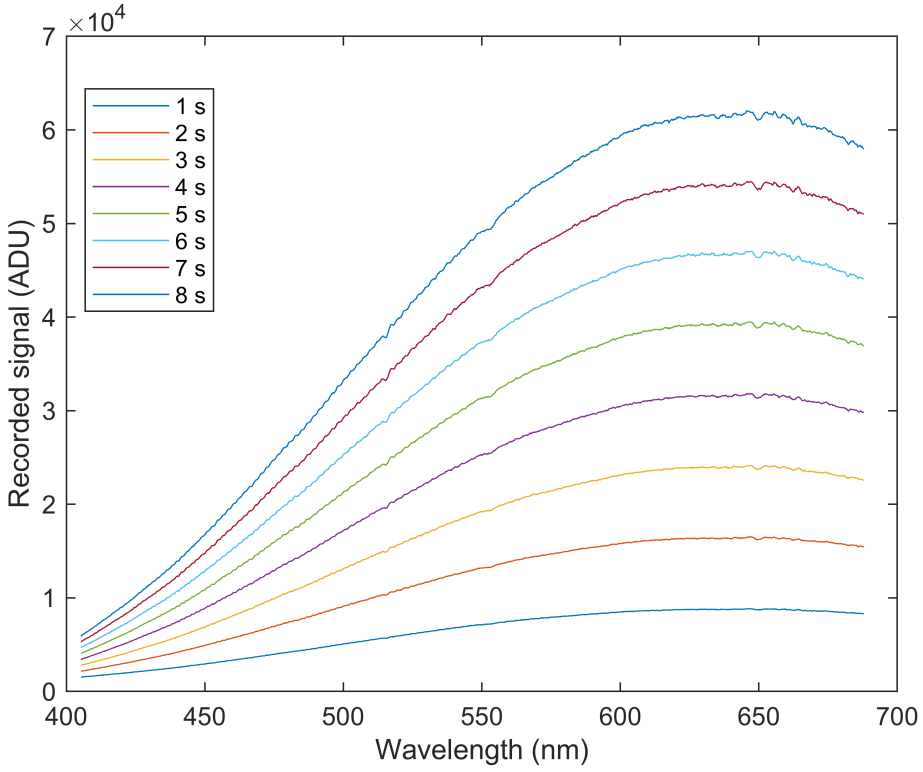


Figure 7. Recorded signal from FEL Lamp 1 as a function of wavelength for exposure times ranging from 1 to 8 s. Three ND filters were used to prevent detector saturation.

3.3 Grating 3

A second on-site radiometric calibration campaign was carried out in October 2024 to characterize Grating 3. Owing to its higher spectral dispersion, the optical configuration used for Grating 1 did not provide sufficient flux when the three-filter ND assembly was inserted. The calibration setup was therefore modified by replacing the combined ND filters with a single ND200 filter. Its wavelength-dependent transmittance was characterized independently at the B.RCLab and is shown in Figure 9.

The same FEL Lamp 2 was used for the calibration. During the campaign, however, the power supply entered safe mode when operated at the nominal current of 8 A. The lamp was consequently operated at 7 A. To preserve traceability to its 8 A spectral-irradiance calibration, the wavelength-dependent ratio between the lamp irradiances at 7 A and 8 A, $C_{7/8}(\lambda) = E_{7\,\mathrm{A}}(\lambda)/E_{8\,\mathrm{A}}(\lambda)$ was measured independently at the B.RCLab. The reference spectral irradiance at 8 A was then corrected using this ratio to obtain the irradiance corresponding to the 7 A operating current. The spectral irradiance of the calibration lamp was obtained using equation 2 with $E_{\mathrm{lamp}}(\lambda) = E_{8\mathrm{A}}\, C_{7/8}(\lambda)$ and $T_{\mathrm{ND}}(\lambda) = T_{\mathrm{ND200}}$.

https://doi.org/10.5194/egusphere-2026-5344
Preprint. Discussion started: 18 November 2026
© Author(s) 2026. CC BY 4.0 License.

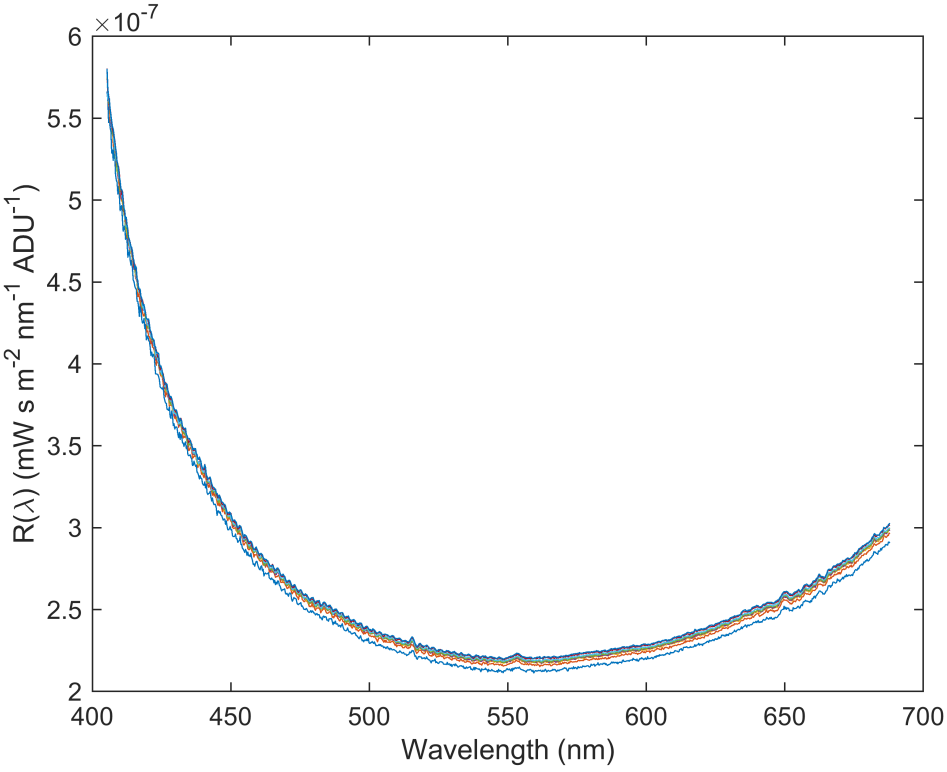


Figure 8. Calibration curves obtained for Grating 1 using FEL Lamp 1 operated at 8 A, for exposure times ranging from 1 to 8 s.

Seven spectral ranges were calibrated for Grating 3. Here, we illustrate the procedure for spectral range 1, covering approximately 407.6–447.5 nm and centered on the N_2^+ first negative emission near 427.8 nm. Calibration curves were independently derived from exposures of 1, 1.5, 2, 4, and 8 s. As shown in Figure 10, the five curves agree closely over the complete spectral range, demonstrating both the linearity of the detector response over these exposure times and the consistency of the calibration procedure.

3.4 Conversion to absolute spectral brightness (Rayleighs)

Using the radiometric response curve derived for the corresponding grating and spectral range, raw detector counts are first converted into spectral radiant exposure in $\mathrm{W\,s\,m^{-2}\,nm^{-1}}$, i.e. the time-integrated spectral irradiance at the detector. The calibration accounts for the throughput of the telescope, fiber injection, slit, spectrograph optics, and detector response. The acrylic dome, which was not present during the calibration measurements, is accounted for separately through its transmittance T_d. Losses associated with the finite fiber-slit coupling are thus included in the instrumental response and are not corrected separately.

https://doi.org/10.5194/egusphere-2026-5344
Preprint. Discussion started: 18 November 2026
© Author(s) 2026. CC BY 4.0 License.

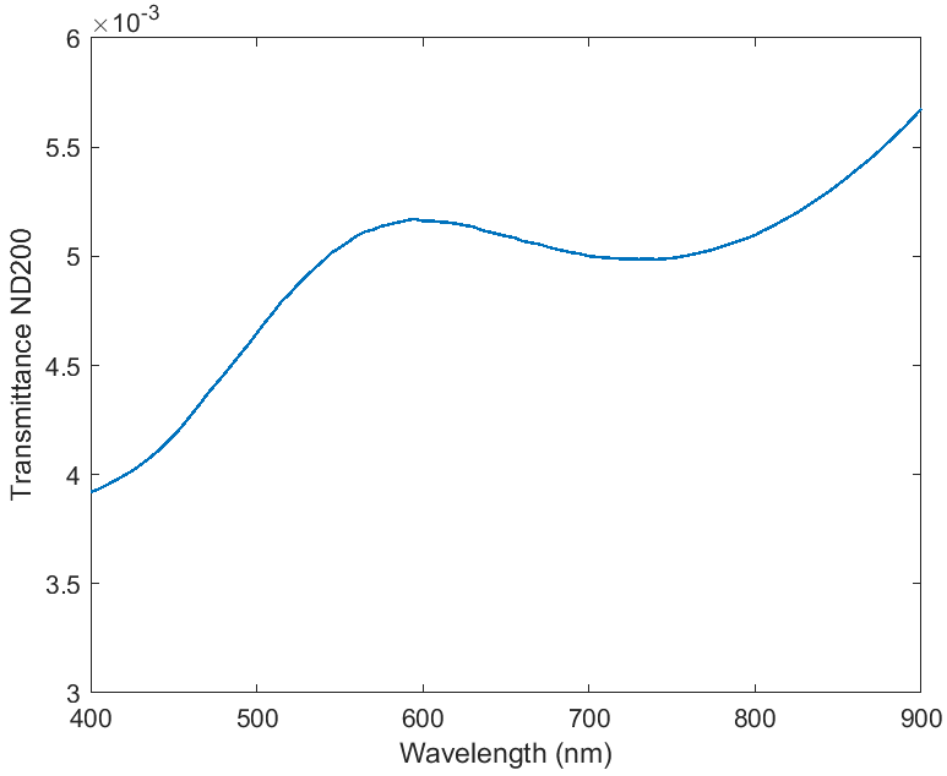


Figure 9. Measured wavelength-dependent transmittance of the ND200 filter used during the radiometric calibration of Grating 3.

The spectra are converted to spectral irradiance in $\mathrm{W\,m^{-2}\,nm^{-1}}$ by dividing by the 30 s exposure time, and then to spectral photon irradiance using $E_\gamma = hc/\lambda$. To convert this quantity to Rayleighs (R), the auroral emission is assumed to be spatially uniform over the ASIS field of view, approximated as a circular cone with a full opening angle $\alpha = 4°$. The corresponding solid angle is $\Omega = 2\pi(1 - \cos\frac{\alpha}{2})$. The spectral brightness is therefore

$$I_R(\lambda) = \Phi_\lambda \frac{4\pi}{10^{10}\Omega}, \tag{3}$$

where Φ_λ is the spectral photon irradiance in photons $\mathrm{s^{-1}\,m^{-2}\,nm^{-1}}$, and $I_R(\lambda)$ is the spectral radiance expressed in $\mathrm{R\,nm^{-1}}$. This approximation is appropriate for diffuse auroral emissions and yields a field-of-view-averaged spectral brightness otherwise.

https://doi.org/10.5194/egusphere-2026-5344
Preprint. Discussion started: 18 November 2026
© Author(s) 2026. CC BY 4.0 License.

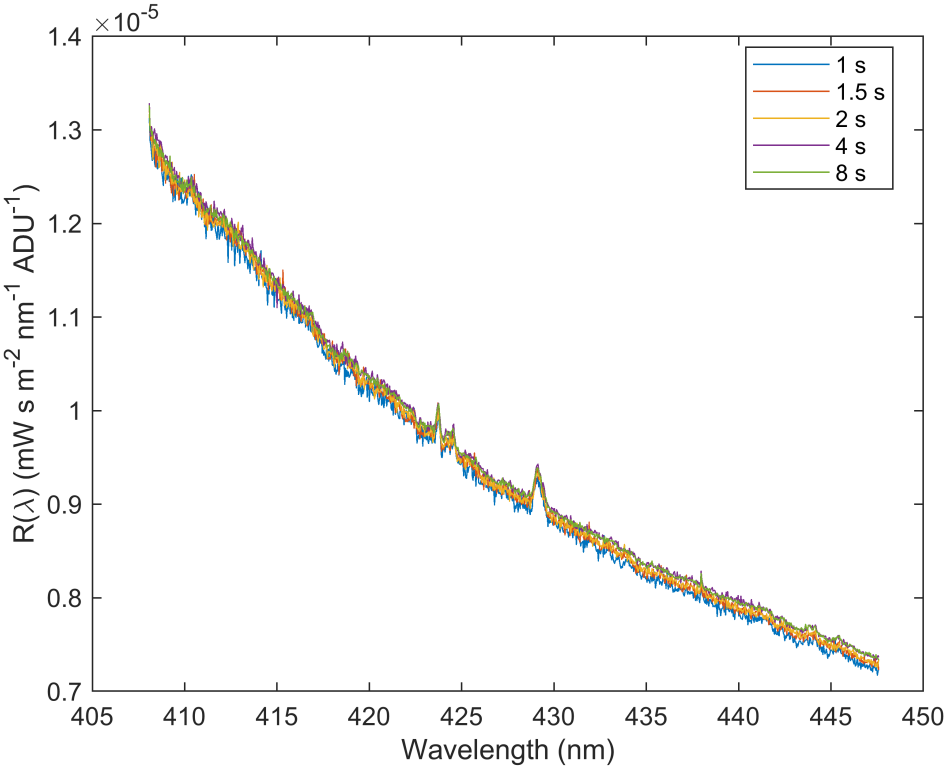


Figure 10. Calibration curves obtained for Grating 3 using FEL Lamp 2 operated at 7 A, for exposure times ranging from 1 to 8 s.

4 Wavelength calibration

4.1 Grating 1

Wavelength calibration was performed using two spectral calibration lamps from Ocean Optics, both equipped with SMA connectors for direct coupling to the optical fiber. The first lamp (Hg-1) is a mercury–argon source providing strong emission lines in the blue region of the visible spectrum. The second lamp (Ne-1) is a neon source optimized for the red part of the visible spectrum, particularly in the [540–754] nm range.

First, the wavelength range used for observations, [405–687] nm, was considered. More than 30 emission lines were identified using reference data from the National Institute of Standards and Technology (NIST). A second-order polynomial fit was then applied, yielding the following relationship between wavelength λ and pixel number p:

$$\lambda = 405.033 + 0.278\, p - 1.679 \times 10^{-6}\, p^2 \tag{4}$$

https://doi.org/10.5194/egusphere-2026-5344
Preprint. Discussion started: 18 November 2026
© Author(s) 2026. CC BY 4.0 License.

The result is shown in Figure 11, where the measured line positions are displayed as dots and the polynomial fit as the red curve. For comparison, the automatic calibration provided by the spectrograph dashboard is also shown. This built-in calibration is obtained by interactively selecting emission-line peaks and entering their corresponding wavelengths. The two
210 calibration curves are nearly parallel. The small offset (=7 nm) between them likely arises from minor mechanical variations that shift the spectrum on the detector, for example due to slight misalignment of the camera or the grating turret.

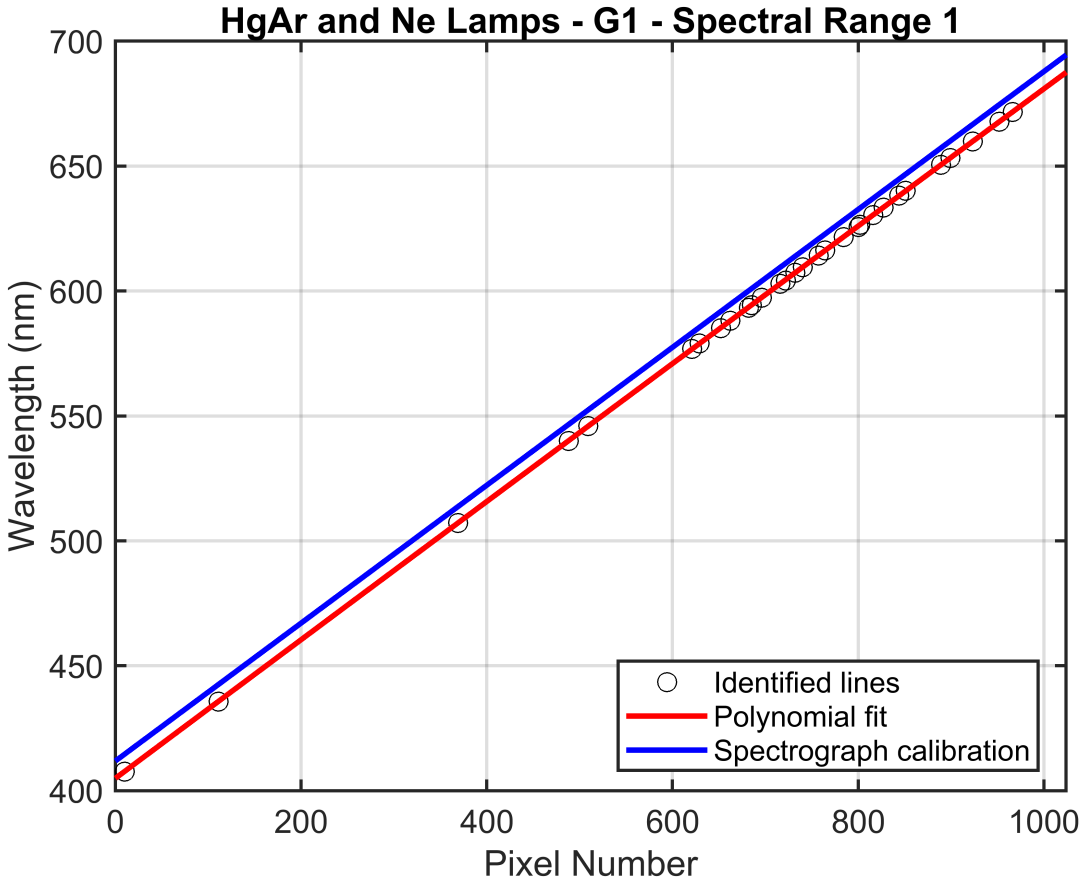


Figure 11. Wavelength calibration curves in the range [405–687] nm. The black dots represent manually identified emission lines from the HG-1 and Ne-1 spectral lamps. The red curve shows the second-order polynomial fit derived from these measurements. The blue curve corresponds to the linear dispersion relation automatically provided by the SR-303i spectrograph control software, based on the factory calibration.

Another wavelength range was investigated, extending further into the red part of the spectrum: [519–800] nm, with a central wavelength $\lambda_c = 660.27$ nm. The following second-order polynomial fit was found:

$$\lambda = 511.830 + 0.277\, p - 3.248 \times 10^{-6}\, p^2 \tag{5}$$

https://doi.org/10.5194/egusphere-2026-5344
Preprint. Discussion started: 18 November 2026
© Author(s) 2026. CC BY 4.0 License.

215 The corresponding wavelength calibration curve is shown in Figure 12, exhibiting the same constant offset as previously observed. The fact that the calibration curves remain parallel over both wavelength ranges supports the validity and consistency of the calibration procedure.

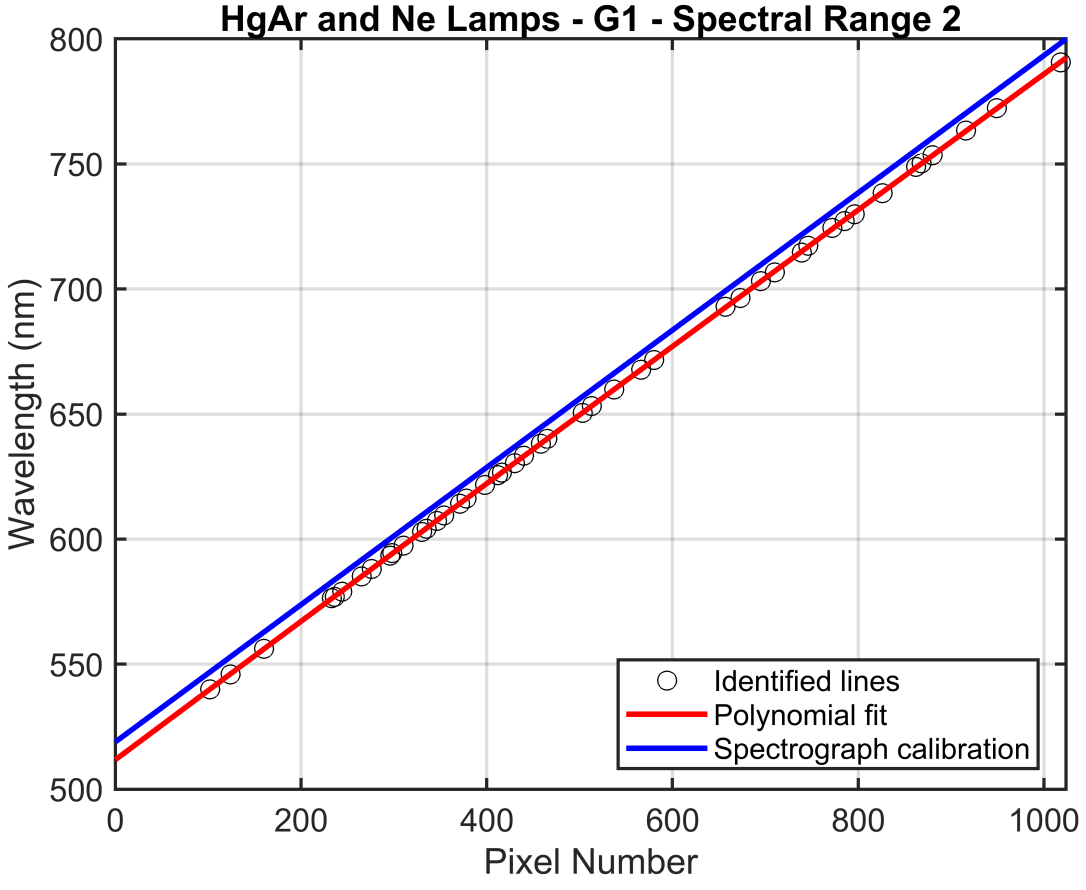


Figure 12. Wavelength calibration curves in the range [519–800] nm using the HG-1 and Ne-1 spectral lamps. The dots and red curve correspond to a polynomial fit of the manually identified emission lines while the blue curve is a linear variation provided automatically by the dashboard controlling the SR-303i spectrograph and corresponding to a factory calibration.

4.2 Grating 3

Grating 3 with 1800 lines mm^{-1} provides higher-resolution spectra to resolve specific auroral emission lines during dedicated
220 campaigns. Its spectral dispersion is $\frac{d\lambda}{dp} \sim 0.05\ \mathrm{nm\,pixel}^{-1}$.

During the wavelength calibration campaign, seven spectral ranges were selected including the following emission lines: 427.8 nm (N_2^+ 1NG), 510.0 nm (region with several bands of N_2 2P), 557.7 nm ($O(^1S \rightarrow {}^1D)$), 630.0 nm ($O(^1D \rightarrow {}^3P_2)$),

https://doi.org/10.5194/egusphere-2026-5344
Preprint. Discussion started: 18 November 2026
© Author(s) 2026. CC BY 4.0 License.

636.4 nm ($O(^1D \rightarrow {}^3P_1)$), 656.3 nm ($H_\alpha$), 732.0 nm (doublet O^+ $(^2D \rightarrow {}^2P)$), and 777.4 nm (multiplet $O\,(3p^5P \rightarrow 3s^5S^o)$).

Because each spectral window spans only about 40 nm, relatively few calibration lines are available within a single exposure. To increase the number of identifiable lamp lines, the exposure time was intentionally increased so that weaker emission lines became detectable, while the brightest lines were allowed to saturate. This strategy typically provided more than ten emission lines for the wavelength calibration of each spectral range.

As an illustration, for the spectral range 1 (centred on the N_2^+ 1NG emission at 427.8 nm), the following second-order polynomial fit was found:

$$\lambda = 408.046 + 0.040\,p - 1.354 \times 10^{-6}\,p^2 \tag{6}$$

The corresponding wavelength calibration curve is shown in Figure 13, exhibiting a different constant offset than previously observed. The change in the constant offset simply reflects the different optical configuration associated with Grating 3.

As an example of ASIS performance in the blue spectral range, Figure 14 shows a radiometrically calibrated auroral spectrum between 415 and 440 nm. The spectrum was obtained by averaging 20 consecutive 60 s exposures, corresponding to a total integration time of 20 min. After dark subtraction and radiometric calibration, the N_2^+ first negative (1NG) (0,1) band at 427.8 nm is clearly detected, together with the weaker (1,2) and (2,3) bands at 423.6 and 419.9 nm, respectively.

5 Examples of data and applications

5.1 Geomagnetic Storms and Substorms

During periods of enhanced geomagnetic activity, including geomagnetic storms and substorms, ASIS records a broad range of auroral atomic lines and molecular bands. These intervals provide useful test cases for assessing the spectral capabilities of the instrument, because both the main auroral emissions and weaker spectral features can be detected within the same observations.

An example is shown in Figure 15. The spectrum exhibits clear emissions from the first negative band system of N_2^+ (1NG), as well as from the first positive band system of N_2 (1PG). In addition to the dominant auroral emissions, weaker spectral features are also visible, including the [N I] emission near 520 nm and the [N II] emission near 500 nm. Such spectra provide a direct view of the relative contributions of atomic oxygen, molecular nitrogen, ionized molecular nitrogen, and atomic nitrogen emissions during disturbed geomagnetic conditions.

ASIS is also useful as a ground-based spectroscopic support instrument in broader multi-instrument studies. A recent example is given by Nanjo et al. (2026), where ASIS observations were used together with all-sky imaging, narrow-band optical cameras, a spectral riometer, ground magnetometer measurements, high-speed imaging, and Swarm satellite observations to investigate fragmented aurora-like emissions and picket-fence structures near the poleward edge of the auroral oval. In such studies, imaging data provide the morphology, motion, and spatial context of the aurora, while ASIS provides the spectral identification of the emitting species and their relative intensities.

https://doi.org/10.5194/egusphere-2026-5344
Preprint. Discussion started: 18 November 2026
© Author(s) 2026. CC BY 4.0 License.

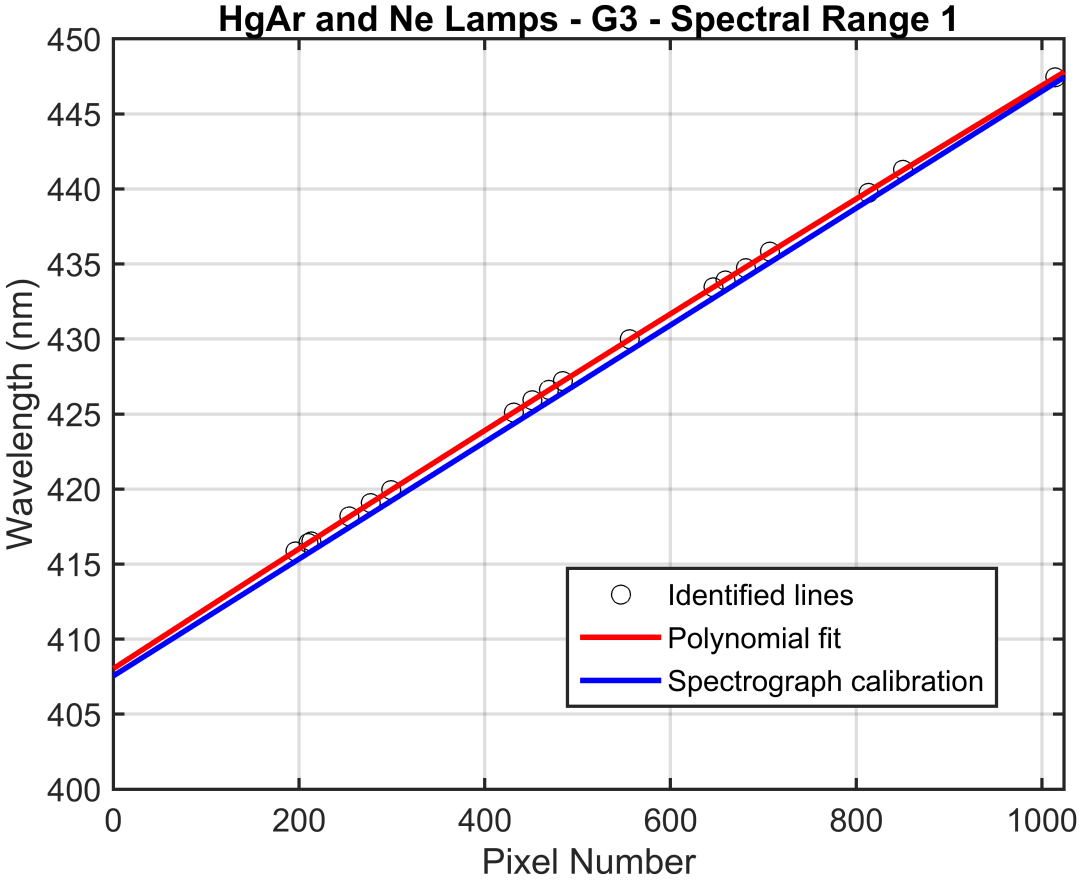


Figure 13. Wavelength calibration curves in the range $[407.6–447.5]$ nm. The black dots represent manually identified emission lines from the HG-1 and Ne-1 spectral lamps. The red curve shows the second-order polynomial fit derived from these measurements. The blue curve corresponds to the linear dispersion relation automatically provided by the SR-303i spectrograph control software, based on the factory calibration.

The continuous ASIS observations also provide calibrated time series of the main auroral emissions (see Figure 16). These time series make it possible to follow the temporal evolution of the N_2^+ 427.8 nm band, the O(^{1}S) 557.7 nm line, the O(^{1}D) 630.0 and 636.4 nm lines. This temporal information is essential for identifying stable intervals where line-ratio diagnostics can be interpreted physically, and for distinguishing rapidly evolving substorm structures from quieter arcs, diffuse aurora, or mixed precipitation regimes.

5.2 Electron Energy Estimates

Line-intensity ratios can be used as proxies for the characteristic energy of precipitating auroral electrons. In particular, the ratio between red oxygen emissions at 630 nm and blue N_2^+ emissions provides a useful diagnostic of electron precipitation

https://doi.org/10.5194/egusphere-2026-5344
Preprint. Discussion started: 18 November 2026
© Author(s) 2026. CC BY 4.0 License.

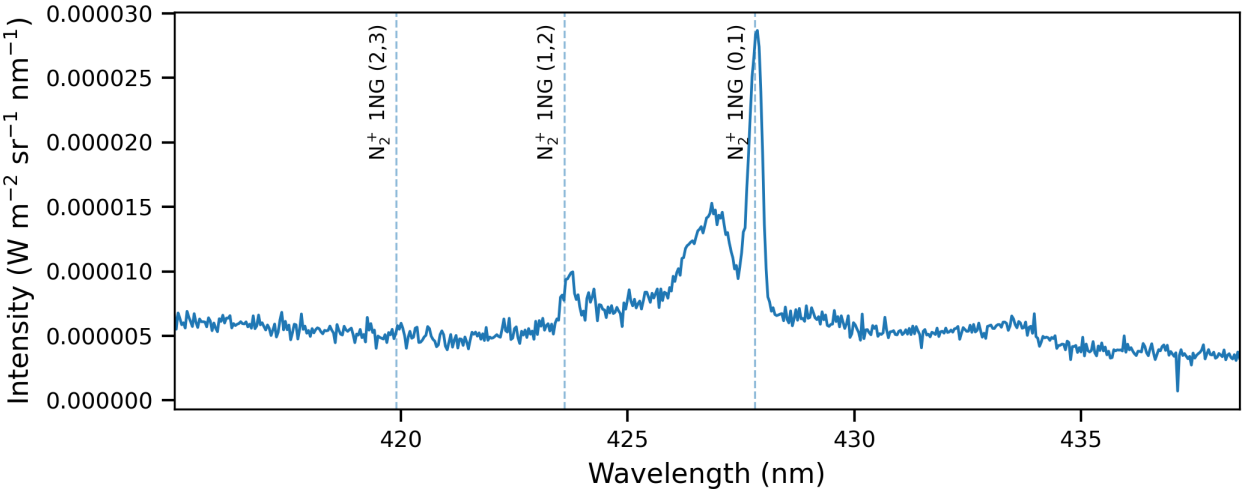


Figure 14. Radiometrically calibrated ASIS spectrum obtained with Grating 3, showing the N_2^+ first negative band heads at 419.9, 423.6, and 427.8 nm

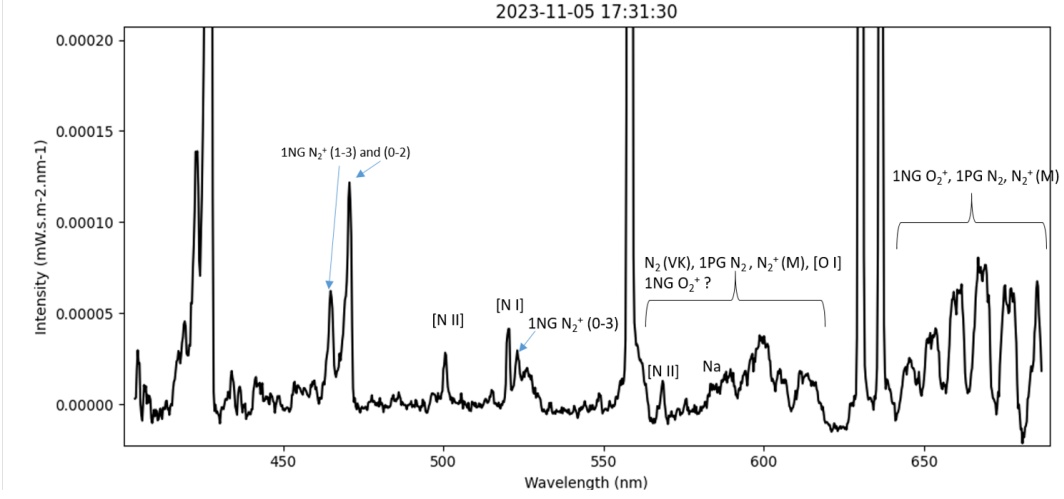


Figure 15. Example of an ASIS spectrum recorded during enhanced geomagnetic activity on the 5th of November 2023.

energy, as illustrated in Figure 16. In this work, the red-to-blue ratio is computed from calibrated and spectrally integrated emissions, rather than from peak intensities alone.

The physical interpretation of this ratio relies on electron transport models. The observed ratios can be compared with look-up tables derived from models such as Transsolo (Barthelemy et al., 2025), using up to 32 streams, or with earlier two-stream calculations such as those of Ono (1993) and Adachi et al. (2017). These models provide the expected auroral emission ratios as a function of the characteristic energy of the precipitating electrons.

https://doi.org/10.5194/egusphere-2026-5344
Preprint. Discussion started: 18 November 2026
© Author(s) 2026. CC BY 4.0 License.

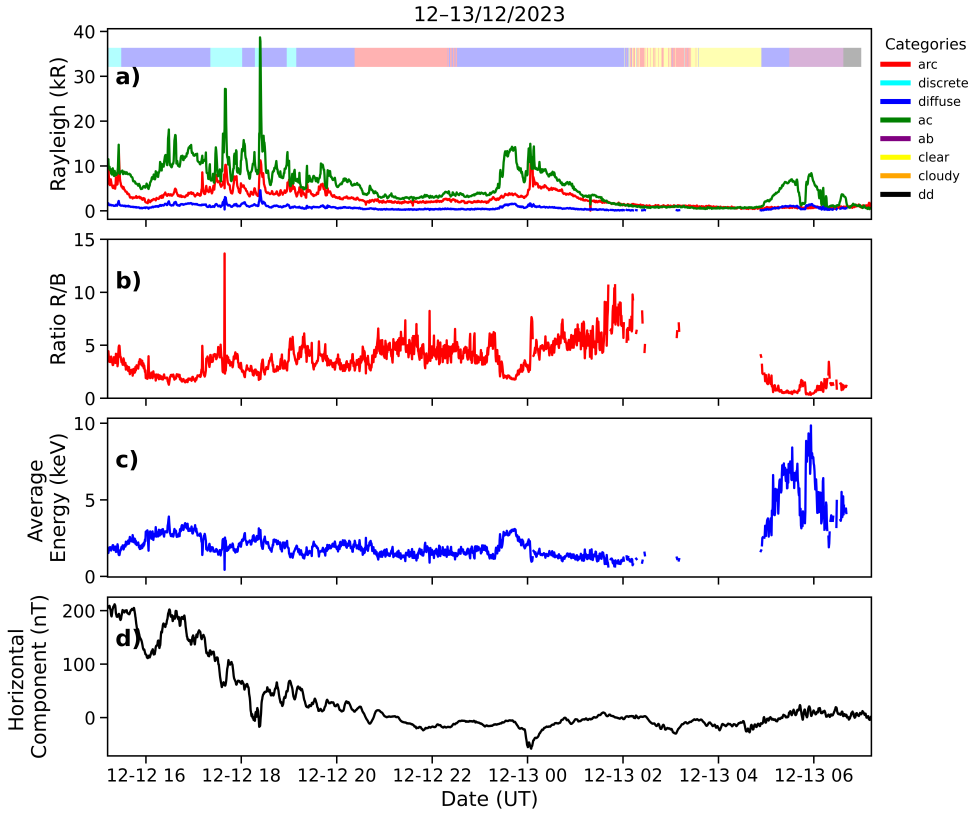


Figure 16. Results from ASIS for 12-13 December 2023. Panel a): green (557.7 nm), red-doublet (630/636 nm), and blue (427.8 nm) intensities, together with the AI-based morphology classification from Nanjo et al. (2022); Panel b): ratio between the 630 nm line emission and the 427.8 nm. Panel c): average energy using the look-up table from Adachi et al. (2017) in blue. Panel d): magnetic disturbance horizontal component from Tromsø magnetic observatory.

The auroral classifications used for Figure 16 follow the machine-learning-based classification results of Nanjo et al. (2022) for the Skibotn all-sky camera. This classification provides an independent morphological context for separating diffuse, pulsating, arc-like, and disturbed auroral conditions. A detailed application of this approach to pulsating aurora and the morning-sector increase of characteristic electron energy is discussed in Cessateur et al. (2026).

A complementary reconstruction approach, based on fitting ASIS spectra with synthetic spectra generated by the Transsolo electron transport model, is currently being developed to retrieve both the total energy flux and the mean energy of the precipitating electron distribution from monitoring-mode spectroscopic observations.

https://doi.org/10.5194/egusphere-2026-5344
Preprint. Discussion started: 18 November 2026
© Author(s) 2026. CC BY 4.0 License.

5.3 Proton Aurora

ASIS also regularly detects spectral signatures associated with proton aurora. These signatures include Balmer emissions, in particular Hα and Hβ as shown in Figure 17.

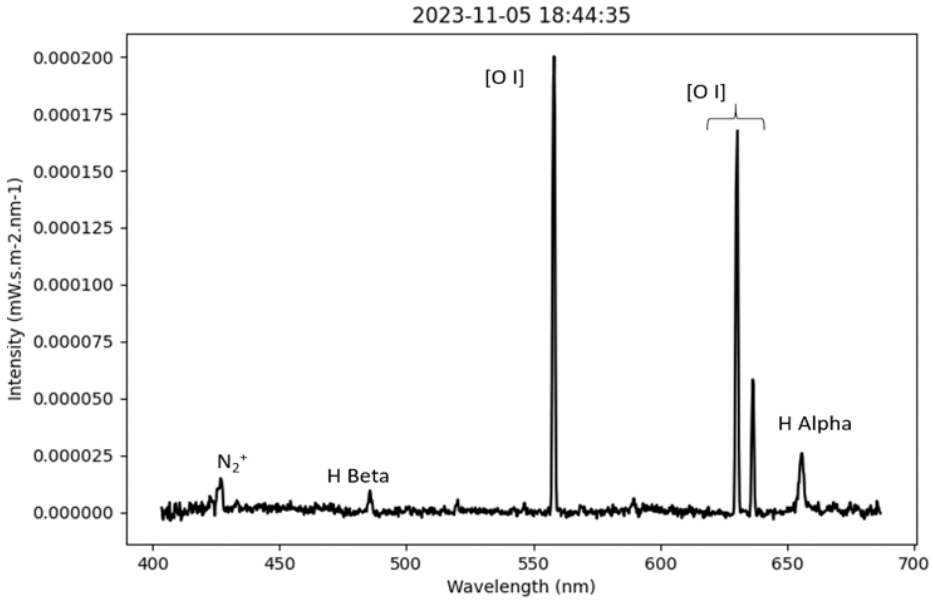


Figure 17. Example of an ASIS spectrum showing Balmer emissions associated with proton aurora on 5 November 2023. The Hβ and Hα lines are detected together with the main electron-auroral emissions, including the N_2^+ band near 427.8 nm, the O(^{1}S) green line at 557.7 nm, and the O(^{1}D) red lines at 630.0 and 636.4 nm. The simultaneous presence of Balmer and oxygen/nitrogen emissions suggests a mixed proton and electron precipitation regime.

Proton aurora is produced when precipitating magnetospheric protons, typically with energies in the keV to tens-of-keV range, interact with the upper atmosphere. Charge-exchange reactions can produce fast neutral hydrogen atoms, which may subsequently radiate through the Balmer series. Because these neutral hydrogen atoms are no longer constrained by the geomagnetic field, proton aurora can have spatial and spectral characteristics that differ from purely electron-driven aurora (Galand and Chakrabarti, 2006).

6 Conclusions

ASIS is a ground-based auroral spectrograph designed for continuous monitoring of visible auroral emissions at Skibotn Observatory. In its standard configuration, Grating 1 provides spectral coverage over approximately 405-687 nm with a spectral resolution of about 1.2 nm, while Grating 3 provides higher spectral dispersion for dedicated observations of selected auroral emission features.

https://doi.org/10.5194/egusphere-2026-5344
Preprint. Discussion started: 18 November 2026
© Author(s) 2026. CC BY 4.0 License.

The instrument has been characterized through both wavelength and radiometric calibration campaigns. Absolute radiometric response curves were obtained using calibrated FEL lamps, with grating-specific calibration configurations adapted to the different optical throughput and spectral dispersion. The consistency of the response obtained for different exposure times demonstrates the stability and linearity of the calibration procedure. Together with the wavelength calibration, these measurements allow ASIS spectra to be expressed in absolute spectral brightness units and therefore used for quantitative auroral studies.

The observations presented here illustrate several scientific applications of ASIS. The instrument resolves the main atomic and molecular auroral emissions during disturbed geomagnetic conditions, provides calibrated line intensities and ratios that can be used to constrain the characteristic energy of precipitating electrons, and detects Balmer emissions associated with proton precipitation. Its continuous operation also makes ASIS well suited for coordinated studies with all-sky imaging, radar, magnetometer, and satellite observations. Further developments based on comparisons with synthetic spectra from electron transport models will extend these measurements towards the quantitative retrieval of precipitating particle energy fluxes and characteristic energies.

Code and data availability. The MATLAB codes and associated data used to derive the response curves and generate the figures presented in this study are available at https://asis.aeronomie.be/UploadDir/Data_and_Codes_for_Article_ASIS.zip.

Author contributions. Hervé Lamy coordinated the study, contributed to the installation and calibration of the ASIS instrument, developed the MATLAB analysis codes, and wrote the manuscript. Gaël Cessateur contributed to the installation of ASIS and to the preparation of the manuscript. David Bolsée contributed to the radiometric calibration of the instrument and performed the laboratory characterization of the calibration sources and neutral-density filters. He also contributed to the preparation of the manuscript. Mathieu Barthélemy contributed to the installation of the instrument and reviewed the manuscript. Magnar Gullikstad Johnsen provided access to the Skibotn Observatory, supported the long-term operation of ASIS, and reviewed the manuscript. All authors discussed the results and approved the final version of the manuscript.

Competing interests. The authors declare that they have no conflict of interest.

Acknowledgements. The procurement of material for ASIS and its installation were partly supported by the Solar-Terrestrial Centre of Excellence (STCE; https://stce.be). Gaël Cessateur also received support from the PRODEX project SoMA-SMILE (contract 4000151820). We thank Dr. S. Nanjo for providing the all-sky image shown in Fig. 2. Artificial intelligence tools were used to improve the English, check consistency throughout the manuscript, and enhance the readability of the MATLAB codes. OpenAI's ChatGPT image-generation tool was

https://doi.org/10.5194/egusphere-2026-5344
Preprint. Discussion started: 18 November 2026
© Author(s) 2026. CC BY 4.0 License.

used to prepare the illustrative representation of the instrument in Fig. 1 and to assist in the preparation of the photographic composite in Fig. 4, based on photographs supplied by the authors. The scientific and instrumental content was reviewed by the authors.

https://doi.org/10.5194/egusphere-2026-5344
Preprint. Discussion started: 18 November 2026
© Author(s) 2026. CC BY 4.0 License.

References

Adachi, K., Nozawa, S., Ogawa, Y., Brekke, A., Hall, C., and Fujii, R.: Evaluation of a method to derive ionospheric conductivities using two auroral emissions (428 and 630 nm) measured with a photometer at Tromsø (69.6°N), Earth, Planets and Space, 69, 90, https://doi.org/10.1186/s40623-017-0677-4, 2017.

Barthelemy, M., Lamy, H., Vialatte, A., Johnsen, M. G., Cessateur, G., and Zaourar, N.: Measurement of the polarisation in the auroral N_2^+ 427.8 nm band, Journal of Space Weather and Space Climate, 9, A26, https://doi.org/10.1051/swsc/2019024, 2019.

Barthelemy, M., Robert, E., and Lamy, H.: Synthetic spectra of the aurora: N2, N2+, N, N+, O2+ and O emissions, J. Space Weather Space Clim., 15, 19, https://doi.org/10.1051/swsc/2025013, 2025.

Cessateur, G., Hosokawa, K., Lamy, H., Nanjo, S., Barthelemy, M., Johnsen, M. G., and Maggiolo, R.: Mean Energy variation of Diffuse Aurora Observed with the ASIS Spectrograph, EGUsphere, 2026, 1–19, https://doi.org/10.5194/egusphere-2026-385, 2026.

Chakrabarti, S. et al.: HiTIES: A High Throughput Imaging Echelle Spectrograph for ground-based visible airglow and auroral studies, Journal of Geophysical Research, 106, 30 337–30 348, https://doi.org/10.1029/2001JA001105, 2001.

Chamberlain, J. W.: Physics of the Aurora and Airglow, Academic Press, New York, 1961.

Conde, M. and Smith, R. W.: Mapping thermospheric winds in the auroral zone, Geophysical Research Letters, 22, 3019–3022, https://doi.org/10.1029/95GL02437, 1995.

Conde, M. and Smith, R. W.: Phase compensation of a separation scanned, all-sky imaging Fabry Perot spectrometer for auroral studies, Applied Optics, 36, 5441–5450, https://doi.org/10.1364/AO.36.005441, 1997.

Galand, M. and Chakrabarti, S.: Proton aurora observed from the ground, Journal of Atmospheric and Solar-Terrestrial Physics, 68, 1488–1501, https://doi.org/10.1016/j.jastp.2005.04.013, 2006.

Gillies, D. M., Donovan, E., Hampton, D. L., et al.: First Observations from the TREx Spectrograph: the Optical Spectrum of STEVE and the Picket Fence Phenomena, Geophysical Research Letters, 46, 7207–7213, https://doi.org/10.1029/2019GL083272, 2019.

Nanjo, S., Kataoka, R., Nishiyama, T., Yoneda, M., and Miyaoka, H.: Automatic classification of auroral morphology from all-sky images by using a convolutional neural network, Scientific Reports, 12, 7883, https://doi.org/10.1038/s41598-022-11686-8, 2022.

Nanjo, S., Herlingshaw, K., Sergienko, T., Cessateur, G., Partamies, N., Johnsen, M. G., Hosokawa, K., Lamy, H., Ogawa, Y., Kero, A., Oyama, S., and Yamauchi, M.: Observations of fragmented aurora-like emissions and picket fence on the poleward edge of the auroral oval, Annales Geophysicae, 44, 63–84, https://doi.org/10.5194/angeo-44-63-2026, 2026.

Ono, T.: Derivation of Energy Parameters of Precipitating Auroral Electrons by Using the Intensity Ratios of Auroral Emissions, Journal of geomagnetism and geoelectricity, 45, 455–472, https://doi.org/10.5636/jgg.45.455, 1993.

Partamies, N., Dayton-Oxland, R., Herlingshaw, K., Virtanen, I., Gallardo-Lacourt, B., Syrjäsuo, M., Sigernes, F., Nishiyama, T., Nishimura, T., Barthelemy, M., Aruliah, A., Whiter, D., Mielke, L., Grandin, M., Karvinen, E., Spijkers, M., and Ledvina, V. E.: First observations of continuum emission in dayside aurora, Annales Geophysicae, 43, 349–367, https://doi.org/10.5194/angeo-43-349-2025, 2025.

Rees, M. H.: Physics and Chemistry of the Upper Atmosphere, Cambridge University Press, Cambridge, https://doi.org/10.1017/CBO9780511573118, 1989.

Tsuda, T. T. et al.: OI 630.0-nm and N2 1PG Emissions in Pulsating Aurora Events Observed by an Optical Spectrograph at Tromsø, Norway, Journal of Geophysical Research: Space Physics, 125, https://doi.org/10.1029/2020JA028250, 2020.

Vallance Jones, A.: Aurora, D. Reidel Publishing Company, Dordrecht, https://doi.org/10.1007/978-94-010-2099-2, 1974.